



## Analysis of fractures in boreholes of the Hot Dry Rock project at Soultz-sous-Forêts (Rhine graben, France)

Chrystel Dezayes, Thierry Villemin, Albert Genter, Hervé Traineau, Jacques Angelier

### ► To cite this version:

Chrystel Dezayes, Thierry Villemin, Albert Genter, Hervé Traineau, Jacques Angelier. Analysis of fractures in boreholes of the Hot Dry Rock project at Soultz-sous-Forêts (Rhine graben, France). Scientific Drilling, 1996, 5, pp.31-41. hal-03997382

**HAL Id: hal-03997382**

**<https://brgm.hal.science/hal-03997382>**

Submitted on 20 Feb 2023

**HAL** is a multi-disciplinary open access archive for the deposit and dissemination of scientific research documents, whether they are published or not. The documents may come from teaching and research institutions in France or abroad, or from public or private research centers.

L'archive ouverte pluridisciplinaire **HAL**, est destinée au dépôt et à la diffusion de documents scientifiques de niveau recherche, publiés ou non, émanant des établissements d'enseignement et de recherche français ou étrangers, des laboratoires publics ou privés.

## Analysis of fractures in boreholes of the Hot Dry Rock project at Soultz-sous-Forêts (Rhine graben, France)

CH. Dezayes<sup>1</sup>, T. Villemin<sup>1</sup>, A. Genter<sup>2</sup>, H. Traineau<sup>2</sup> and J. Angelier<sup>3</sup>

<sup>1</sup> Laboratoire de Géodynamique & U.R.A. C.N.R.S. 69, Université de Savoie, 73376 Le Bourget du Lac, France

<sup>2</sup> BRGM, Direction de la Recherche, Département Géophysique et Imagerie Géologique, BP 6009, 45060 Orléans Cedex 2, France

<sup>3</sup> Laboratoire de Tectonique Quantitative, Université P. & M. Curie, Boîte 129, 75252 Paris Cedex 5, France

**Abstract.** The Hot Dry Rock (HDR) geothermal drill site is located in the Upper Rhine Graben at Soultz-sous-Forêts (Alsace, France). Two boreholes reach a highly fractured basement of porphyritic granite, potential site for a geothermal reservoir. Data from the striated faults observed on cores enabled us to compute the paleostress tensors corresponding to the tectonic regimes that affected the granite. Four stress states have thus been determined: a N20°E compression, an N100°E extension, a N80°E compression and a N120°E compression. Both natural and induced fractures were recognised in cores. The mean strike of natural fractures changes progressively with depth from N170°E to N200°E. These fractures form conjugate systems and their dip direction average N70°E and N270°E (natural fractures) and N100°E-110°E and N270°E (induced fractures). The main orientations of fractures analysed from the borehole images are similar to those deduced from core analysis, but with less dispersion. The four stress states computed with striated faults correspond to the regional tectonic history. The direction of the last compression corresponds to the present-day horizontal maximum stress axis, as suggested by the orientation of induced fractures identifiable on the borehole images. A rotation of the core-induced fractures with depth is probably due to stress perturbation related to the presence of an important fault close to the geothermal drillsite.

reservoir, the knowledge of both the fracture pattern in the granite and the orientation of the present-day stress field is required. As a result, extensive analyses of 3-D fracture patterns and stress regimes were undertaken.

The drill site at Soultz-sous-Forêts is located on a significant positive thermal anomaly, near the old Pechelbronn oil field (Fig. 1). Numerous subsurface data are available, resulting in an excellent structural knowledge of the Oligocene extensional structure (Schnaebelé, 1948). The temperature at the depth of

### Introduction

The porphyritic granite underlying the Tertiary of the upper Rhine Graben offers potential sites for geothermal reservoir. Geothermal exploitation would involve creating a heat exchanger between two deep boreholes 500 m apart. Fresh water, injected into one borehole will be recovered hot from the other. The determination of fracture permeability and potential for hydraulic fracturing plays a major role in the geothermal investigation. To design this

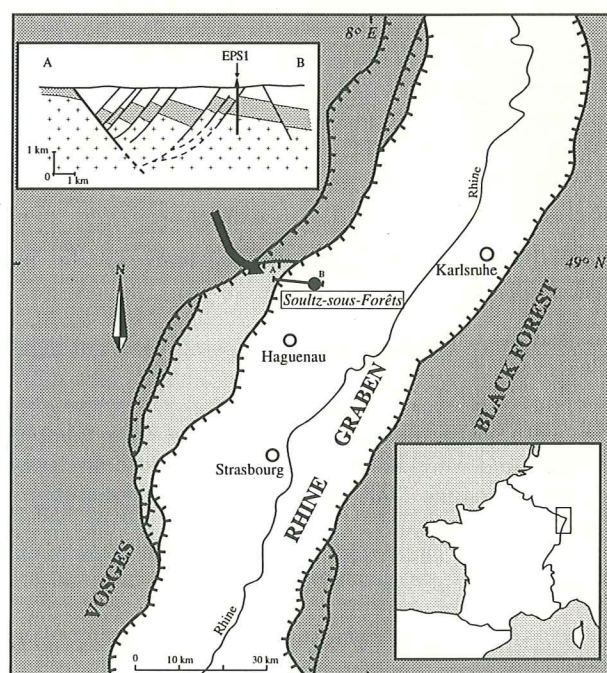


**Fig. 1** : Location of the geothermal drill site of Soultz-sous-Forêts within the Rhine graben. Vertical section AB: cross pattern, granite basement; grey, mesozoic sediments; white, Oligocene and Miocene filling sediments.



2000 m is about 140°C (Schellschmidt and Schulz, 1991), i.e., more than twice the temperature reached with a common geothermal gradient (30°/km). At Soultz, the Hercynian granite was found at a depth of 1400 m, beneath the Mesozoic and Cenozoic strata.

Under the auspices of the European Hot Dry Rock (HDR) program, two deep boreholes were drilled in the upper Rhine Graben at Soultz-sous-Forêts, Alsace, France (Fig. 1). The first borehole, called 'GPK1' (Fig. 2), without coring, was drilled down to 2000 m (Kappelmeyer *et al.*, 1991). The second borehole, called 'EPS1' (Fig. 2), was fully cored to a depth of 2227 m, providing 810 m of granite core (Genter and Traineau, 1992).

In this paper, we describe first the data available, and second the procedures adopted to characterize the fractured environment. Fracture systems have been studied using two methods: direct observation in the cores of the EPS1 borehole, and analysis of borehole imagery in both the GPK1 and EPS1 boreholes. The geometry of the fracture systems has been determined first in terms of the orientations of their multiple fracture sets. This geometrical analysis provided a basis for a better description of the fracture network.

Geometrical analysis, however, is not sufficient in that it does not allow geodynamic understanding directly. For this reason, striation marks visible on fracture planes as indicators of fault slips have been used in a second step, in order to reconstruct the paleostress fields and their succession. Such a technique allows determination of the paleostress regimes. Where faults are newly formed, even where faults are inherited (i. e., reactivated weakness planes such as joints), it also allows predictive determination of the geometry of fracture networks in terms of genetic fracture sets knowing the orientation of paleostress, one infers the orientations of potential conjugate shear fractures as well as tension fractures (Anderson, 1951).

## 1- Fracturation and fault systems in the Soultz boreholes

The EPS1 borehole was fully cored; as a consequence, faults and other fractures in the granite were observed extensively for a depth range of about 800 m (Fig. 2). Furthermore, in both the EPS1 and GPK1 boreholes, fractures were identified and analysed using different borehole image data, BHTV and FMS-4 pads (Fig. 2). It was thus possible to compare the results of direct observation and image analysis in EPS1, then to analyse the sole imagery data of GPK1.

### 1-1 Measurements of faults in cores of the EPS1 borehole

During the drilling of the EPS1 borehole, Genter and Traineau (1991) have established a complete sampling of cores fractures. Thus, they determined the orientation of each fracture as well as the orientation of the associated slip. All fracture orientations were accurately calculated based on the digitalization of the fracture trace on

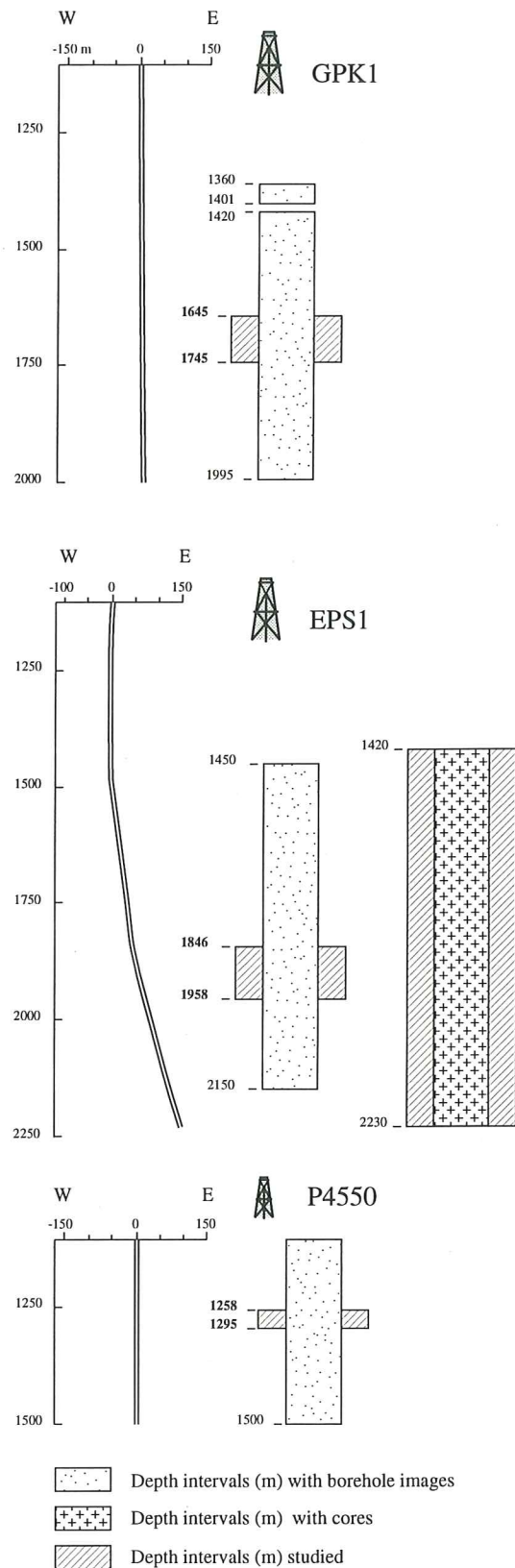


Fig. 2 : Cross-sections oriented E-W in GPK1 borehole, EPS1 borehole and P4550 borehole, representing the different available data and their depth ranges presented in this study.

photocopies of the cylindric outer surface of the core, using the Geological Data Management Software (G.D.M.) of the BRGM. Orientations were first measured in relation to arbitrary coordinate axes: the axis of the borehole is assumed to be vertical, and a line drawn along the core give a relative North. Later, the re-orientation process for each plane (i. e., the determination of the actual dip direction and dip) was accomplished using an intermediate rotation.

The BHTV images (DMT data provided by SWBU) and the corresponding cores of the EPS1 borehole have been compared in detail. Important fractures in BHTV images (types 1 and 2, cf. §1-3-2) effectively correspond to faults or important fractures observable in the cores. This comparison permitted the orientation of cores to be determined as follows: the reference line drawn along all pieces of core that can be put back together, has been adjusted in their relative original position accurately. As the images were oriented using the magnetic North, the orientation of major fractures visible in the core was computed using a rotation matrix, taking into account the trend and plunge of the borehole axis. As a result, the actual dip direction, dip, and slip direction of all fractures were reconstructed.

In summary, the 3-D geometric reconstitution of fracture orientations included two steps: (1) the determination of orientations in an arbitrary reference frame attached to both the drill core axis and the reference line along the core; (2) a correction based on comparison with the BHTV data, taking into account the true borehole orientation. Fracture data were finally obtained in the geographic reference frame.

The EPS1 borehole is noticeably deviated at its base (22° at 2200 m depth); this deviation raises additional problems for computing the orientations and the sense of fault slips from direct core observation (Dezayes, 1992). Note that for paleostress analysis, not only the direction but also the sense of shear on each fault must be known. Shear sense was first determined with the core oriented vertically, top upwards. If the well is strongly deviated, which was the case in their deepest portion for the EPS1 borehole, the real sense of movement may differ from the measured sense. For instance, a normal fault may appear as a reverse fault when the drill core is held vertically (Fig. 3).

The procedure for determining the real sense of motion, elaborated using a spreadsheet (Dezayes, 1992), implies that the normal to the fault and the striae are considered as a set of perpendicular vectors. As a sense convention, the slip vector (parallel to striae) can be chosen as representing the relative motion of the block containing the vector normal to the fault (Fig. 3). The senses of all slip vectors have been chosen in agreement with this convention, so that the correct sense was maintained through rotations in the geometrical correction process described above. This technique allowed reconstitution of the relative senses of slip in the actual position, with the

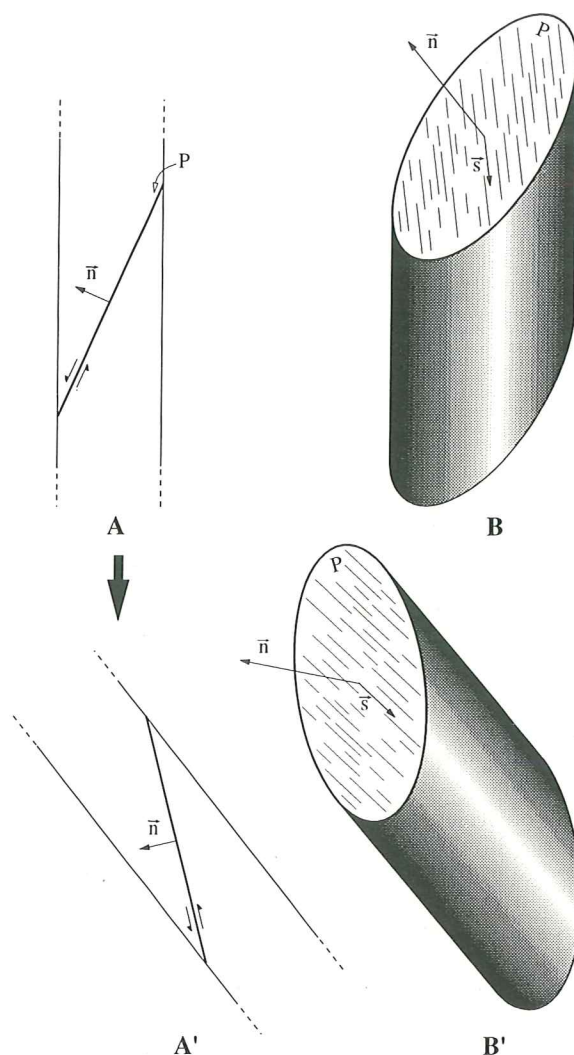


Fig. 3 : Orientation and sense of movement along a fault. A, longitudinal cross-section of a core held in a vertical position. The fault seems to be a normal fault. The vector normal ( $\vec{n}$ ) to fault (P) extends downwards; B, view of the fault plane. The vector representing its striae ( $\vec{s}$ ) indicates the movement of the hanging wall relative to the footwall; A', in the case of a dip fault that is nearly horizontal or vertical (this example), if the deviation changes the dip direction, the sense of movement may change from normal to reverse.

same convention. 141 striated faults have been (Tab. 1) initially oriented by Traineau *et al.* (1992) under the assumption of vertical drill core. The sense of motion of 7 slips, all located near the bottom of the borehole where the greatest deviation occurs, have thus been reversed.

#### 1-2 Fractures in cores of the EPS1 borehole

All cores of the EPS1 borehole were examined and described. Particular attention was paid to the petrographic nature of the granite, its alteration zones and the major discontinuities (Genter and Traineau, 1992). About 4100 fractures were observed and separated into 12 types of natural fractures (older than drilling) and induced fractures



Depth	Shear sense	State of stress	Dip direction	Dip	Pitch of striae
1430.6	R S	A	312	72	6 N
1430.4	N S	A	312	58	9 S
1430.6	N S	B	282	35	44 S
1430.8	N S	A	303	24	24 S
1430.9	R S	A	328	39	17 E
1430.9	N S	A	313	43	59 S
1431.2	N S	E	301	37	11 S
1453.5	R D	A	61	60	60 N
1457.0	R S	D	268	32	41 N
1457.7	N D	E	287	28	49 N
1458.9	* S	D	89	85	0 N
1464.6	N D	B	273	52	61 N
1465.8	N S	B	291	12	82 S
1467.4	R D	A	70	71	9 N
1467.5	N S	B	89	62	51 N
1467.7	R D	A	61	76	24 N
1468.6	R D	A	80	67	20 N
1469.9	R S	E	275	81	48 N
1480.0	R D	D	195	82	83 E
1481.0	N D	C	283	68	30 N
1487.3	R D	A	28	80	6 W
1487.8	N D	B	97	79	43 S
1489.7	R D	A	244	63	13 S
1491.6	N S	B	112	63	57 N
1492.9	N S	E	92	67	22 N
1495.4	R D	A	46	53	40 N
1496.1	R D	A	42	32	57 W
1496.4	N S	E	19	51	56 W
1498.1	N S	B	29	42	80 W
1500.5	R D	A	42	44	37 W
1500.5	R S	C	224	67	60 W
1509.4	N S	C	28	64	35 W
1510.6	R D	D	179	83	23 E
1515.9	N D	A	243	84	40 N
1517.4	N D	B	274	74	57 N
1518.0	R D	C	88	85	39 N
1517.6	N S	B	98	62	51 N
1518.4	R D	E	85	51	89 N
1570.4	N S	A	124	69	42 N
1574.4	N D	B	114	52	77 S
1627.5	N S	B	285	75	66 S
1627.7	N S	B	289	40	70 S
1627.9	N S	B	289	31	66 S
1628.1	N S	B	284	32	59 S
1628.3	N S	B	269	35	76 S
1628.9	N S	B	289	23	61 S
1629.4	R D	D	356	48	23 W
1629.5	N S	A	340	43	14 W
1629.5	R D	C	340	43	29 W
1629.5	N D	D	11	11	5 E
1631.0	R D	C	329	23	62 W
1631.2	R D	C	320	42	20 W
1631.4	N S	A	306	50	24 S
1631.8	N D	B	246	51	85 N
1632.8	R D	D	346	35	1 W
1632.9	R D	D	20	43	10 W
1636.5	N S	E	280	36	31 S
1640.5	N D	B	111	54	84 S
1641.9	N S	B	113	64	68 N
1644.2	N S	A	123	33	63 N
1644.8	N S	B	113	55	74 N
1645.1	N D	A	255	34	36 N
1645.4	R D	C	281	30	80 S
1647.0	N D	B	261	8	75 N
1647.2	N D	E	210	20	16 W
1647.2	R S	E	124	10	11 S
1647.8	N S	A	328	51	35 W
1647.9	N S	D	41	50	59 W
1647.8	R D	A	41	50	17 W
1647.6	N S	B	146	20	66 E

Depth	Shear sense	State of stress	Dip direction	Dip	Pitch of striae
1648.0	N D	A	51	10	22 S
1648.2	R D	D	337	15	71 W
1648.7	R D	D	343	25	42 W
1648.1	N S	E	16	23	39 W
1648.9	N D	B	254	41	89 N
1649.4	N D	B	227	21	69 N
1653.7	N D	B	233	56	64 N
1654.0	N D	B	46	22	84 S
1672.9	R S	E	27	60	62 E
1673.5	N D	E	297	43	41 N
1673.8	R S	C	24	21	34 E
1674.3	N S	D	172	4	28 E
1674.5	N D	B	62	56	71 S
1674.5	R D	A	62	56	14 N
1675.0	N D	A	57	43	20 S
1701.9	N D	B	79	56	55 S
1702.4	N D	A	79	51	33 S
1702.8	N D	B	81	58	84 S
1702.8	R D	A	81	58	15 N
1730.6	N S	A	315	42	59 W
1741.7	N S	E	91	42	9 N
1761.1	R S	E	324	70	53 E
1769.7	N D	B	107	60	74 S
1806.4	N S	B	108	47	57 N
1807.2	R S	D	101	78	78 S
1829.1	N S	B	110	67	71 N
1829.7	N D	B	94	71	64 S
1829.9	N D	B	94	26	64 S
1830.9	N D	B	83	57	71 S
1830.9	N S	E	83	57	38 N
1856.2	N S	A	122	74	51 N
1873.8	N S	A	314	76	68 S
1874.7	N S	A	331	79	10 W
1874.6	R D	A	262	59	13 S
1875.1	N S	B	318	80	70 W
1901.6	R D	A	261	25	27 S
1903.9	N S	A	297	63	75 S
1918.7	N D	B	281	69	53 N
1918.9	N S	E	89	57	21 N
1919.1	N S	D	307	84	76 S
1994.5	N S	E	98	87	45 N
2059.3	R S	E	310	58	70 N
2063.4	N S	E	191	52	67 E
2071.1	N S	B	116	55	66 N
2072.9	N D	C	315	79	33 E
2078.4	* D	C	92	89	0 S
2078.4	R D	C	289	78	23 S
2095.5	N S	A	316	81	87 W
2106.9	R S	D	81	86	27 S
2113.1	R S	A	305	77	38 N
2114.2	N S	A	301	67	67 S
2157.2	N S	D	277	78	10 S
2159.1	N D	B	249	71	56 N
2164.3	N D	C	292	78	5 N
2167.8	R D	C	119	50	17 N
2168.0	* D	C	109	86	0 S
2168.5	N S	C	191	61	6 E
2169.5	N D	C	112	2	47 S
2169.9	N D	C	151	13	54 W
2173.7	R D	C	278	78	40 S
2177.3	R D	C	322	36	18 W
2177.4	R D	E	264	35	58 S
2177.6	R D	C	300	42	25 S
2177.7	R D	C	283	55	42 S
2177.7	R D	A	255	53	10 S
2214.0	N S	D	286	86	45 S
2214.2	N S	A	308	79	5 S
2215.8	N S	E	320	77	13 W
2217.0	N S	A	301	65	18 S
2222.1	N S	B	286	50	69 S

**Table 1** : List of striated faults. First column, depth of the fault intersection in meter. Second column, shear sense on the fault plane, first letter: dip slip sense (N: normal, R: reverse.), second letter: strike slip sense (S: senestral, D: dextral.). Third column, state of stress: A, N-S compression; B: E-W extension; C, NE-SW compression; D, NW-SE compression; E, remaining faults (see fig. 5). Fourth column, dip direction of the fault plane: in degrees from the North to the East. Fifth column, dip of the fault plane in degrees. Sixth column: pitch of the striae on fault plane in degrees and sense of the pitch.

(due to the relaxation of cores). The natural fractures have hydrothermal fillings and include striated faults, joints, open fractures and veins. The induced fractures are fresh, slightly open and without hydrothermal filling (Genter *et al.*, 1994).

### 1-3 Fractures in borehole images

#### 1-3-1 Borehole imagery tools

##### Borehole Televiewer

The Borehole Televiewer (BHTV, DMT data provided by SWBU) provides an acoustic image (impedance + roughness) of the borehole surface. The method consists of aiming an ultrasonic beam at the borehole wall. The reflected beam is analyzed in terms of amplitude and transit time. The amplitude received depends on the reflectivity of the rock, the attenuation of the fluid and the borehole geometry. The BHTV produces a complete 360° acoustic image of the borehole. Amplitude anomalies with a sinusoidal trace are interpreted in terms of planar discontinuities and can be oriented with a magnetometer, which gives the orientation of the beam according to magnetic North (Fig. 4).

##### Formation Micro Scanner

The Formation Micro Scanner (Schlumberger FMS data provided by BRGM) produces an oriented picture of the borehole wall by mapping its conductivity with a dense array of electrodes. The electrical anomalies reflect the effects caused by changing electrolytic conduction of pores or fractures. In this way, high resistivity zones appear white and low resistivity zones appear dark. On this oriented picture, fractures appear as sinusoidal dark traces. With the FMS four-pad tool, about 50% of the drill hole area is covered in a borehole with a diameter of 8 inches.

A new tool, the Formation MicroImager (FMI by Schlumberger), uses the same principle, but has eight pads in order to cover the entire borehole wall, where the diameter is less than 6.25 inches.

#### 1-3-2 Fractures types from borehole images

At the Soultz site, both deep boreholes (GPK1 and EPS1) and one seismic observation well in the Pechelbronn oil field (P4550) have been studied from different images. Whereas in the GPK1 borehole, BHTV, FMS and FMI images were available, only BHTV images were available in the EPS1 borehole and in the "P4550" borehole.

Certain depth intervals of borehole images (Fig. 2), selected for their large fracture density, have been analysed in detail and the orientations of the fractures have been measured from their traces.

Five kinds of fracture have been recognized on the basis of borehole images (Fig. 4):

1- "large" fractures, corresponding to full sinusoids in images. According to the transit time of the BHTV, these fractures are partly open (Fig. 4-A);

2- fractures, with sinusoids not totally visible, which are generally closed;

3- fractures showing only the upper or lower parts of a sinusoid (Fig. 4-B);

4- joints occurring in sets, showing just the central parts of a sinusoid, and forming en échelon sets parallel to the drill hole axis;

5- fractures several meters long, parallel to the axis of drill hole.

From the comparison with the core observation, we could infer that whereas fractures of types 1 and 2 correspond to natural fractures, types 3, 4 and 5 represent fractures induced during the relaxation of the hole wall.

## 2- Fault-fracture data analysis

This section presents the analysis of fracture data collected in the Soultz boreholes from the cores and the images. First, striated fault planes are used to compute paleostress regimes. Second, fractures without striae observed in drill cores and borehole images are analyzed.

### 2-1 Stress computation from striated faults

Stresses have been computed using the complete set of 141 striated faults with known sense of slip, from EPS1. Paleostress analysis was carried out in several steps. First, based on simple geometrical criteria, most faults were grouped into homogeneous sets. Couples of sets form conjugate fault systems, which are easily identifiable based on geometrical analysis and yield the orientation of principal axes of paleostresses. Four systems have been thus recognized.

Second, for each fault system, a stress tensor was computed using the inversion method (Angelier, 1990 and 1991). This method aims at reconstructing an average stress tensor for a large number of faults, in order to explain the observed movements (Angelier, 1979). Provided that the angle between the calculated shear stress and the observed striae for each fault remains small, this method gives reliable results. Not only the orientations of the three principal stress axes  $\sigma_1$ ,  $\sigma_2$  and  $\sigma_3$ , but also the shape ratio ( $\Phi = (\sigma_2 - \sigma_3) / (\sigma_1 - \sigma_3)$ , with  $\sigma_1 > \sigma_2 > \sigma_3$ ) of each tensor are computed. This ratio  $\Phi$  characterizes the shape of the stress ellipsoid (Angelier, 1990). One should note that, to the contrary of geometrical analyse of conjugate faults presented below, this method does not include any assumption about the 'neoformed' or inherited character of each fault slip. As a result, the slip reactivations of randomly oriented weakness planes (e. g., preexisting fractures) are taken into account as well as the development of new faults under a given tectonic stress regime.

In the granite, 85% of the faults can be grouped in four sets of neoformed faults. A residual group of 20 faults corresponds to those which do not belong to any of the these four sets (Fig. 5-E). This residual subset may include some data with possible measurement errors; it also includes all faults which could not be classified according to the model of conjugate faulting. These data



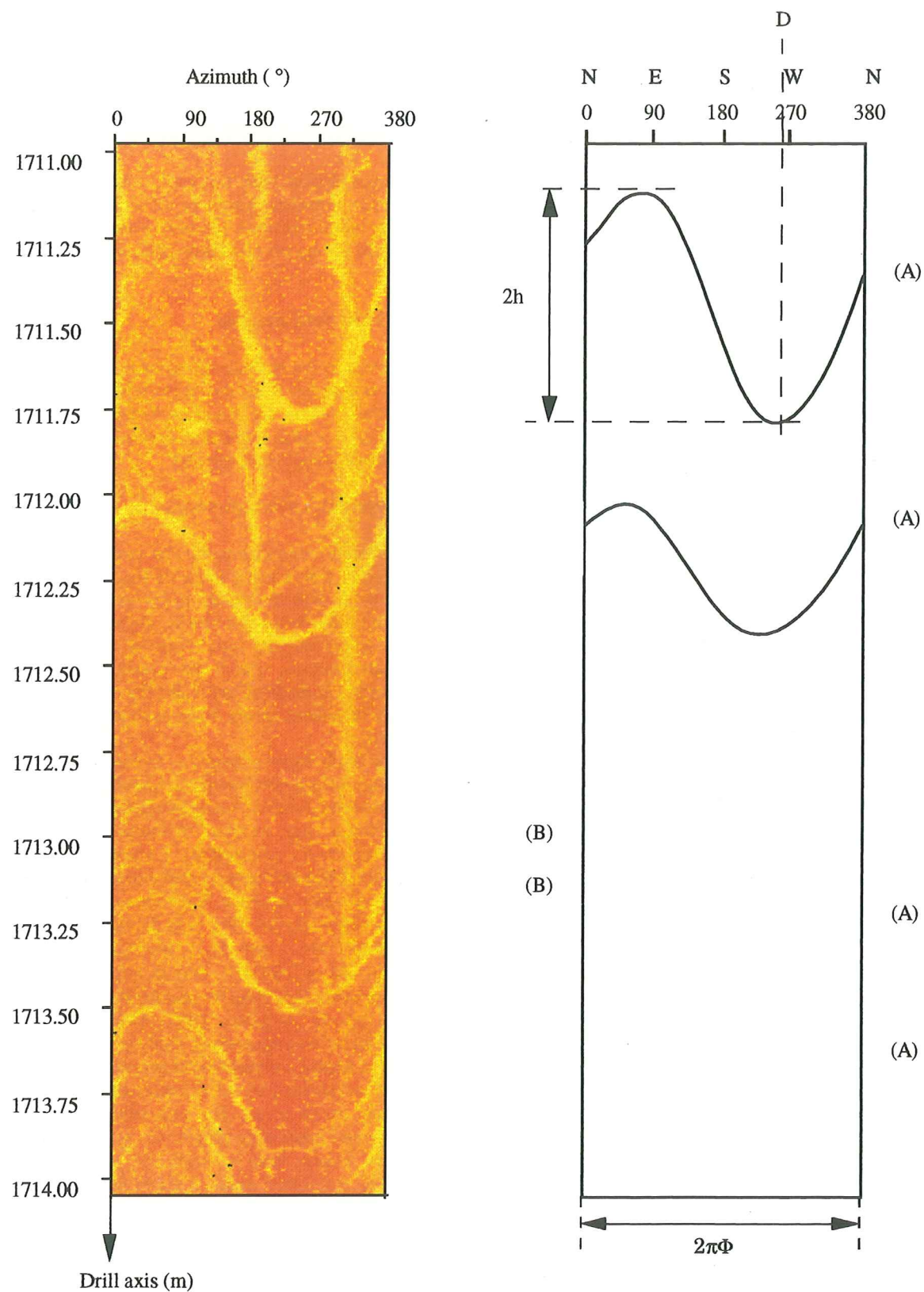


Fig. 4 : Borehole Televiewer image of GPK1 (SABIS system, provided by SWBU) at a depth of 1711 to 1714 m, and its interpretation. (A), important fracture, type 1 ; (B); half fractures, type 4;  $\Phi$ , borehole diameter;  $h$ , amplitude of sinusoid;  $D$ , dip direction of fracture;  $d$ , dip of fracture,  $d = \arctan(2h/\Phi)$ .

may correspond to inherited fault slips, as discussed in a later subsection, and they should be incorporated in the tensor analysis. They were not used in our initial analysis which resulted in the identification of four conjugate sets by pure geometrical means.

The four stress states and corresponding fault sets are as follow (Fig. 5 and Tab. 2):

- nearly N-S compression (Fig. 5-A), well recorded in the granite by 40 N-S strike-slip faults, sinistral faults trending NE-SW and dipping to the West, and dextral ones trending NNW-SSE and dipping to the East. The maximum compressive stress ( $\sigma_1$ ) and the minimum stress ( $\sigma_3$ ) lie approximately in the horizontal plane, whereas the intermediate stress ( $\sigma_2$ ) is nearly vertical.

- E-W extension (Fig. 5-B), deduced from 40 N-S striking conjugate normal faults. In this case,  $\sigma_2$  and  $\sigma_3$  lie approximately in the horizontal plane, while  $\sigma_1$  is nearly vertical. The trends of unclassified stress axes are almost the same as for the regime mentioned above;  $\sigma_1$  and  $\sigma_2$  axes have however been exchanged ( $\sigma_1/\sigma_2$  permutation). As a result, the direction of maximum and minimum horizontal stresses are similar.

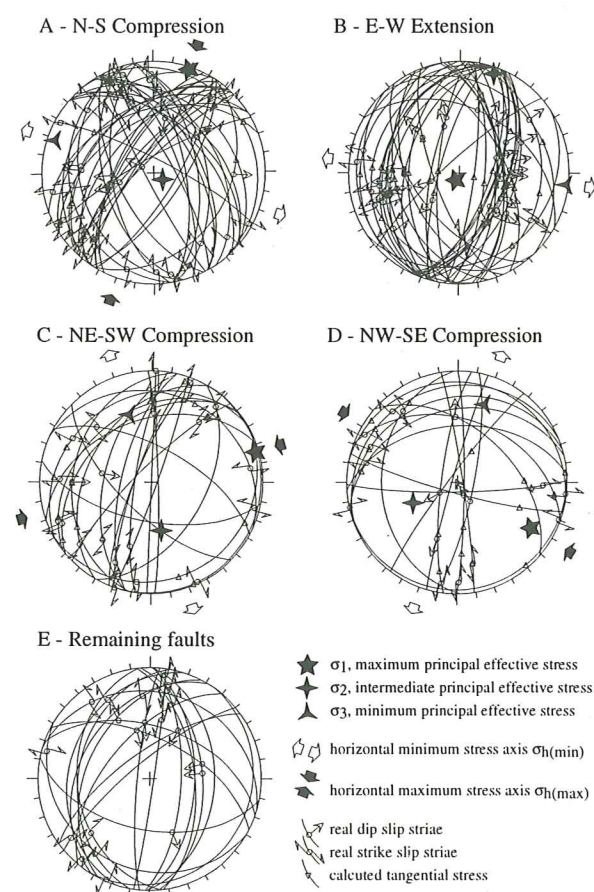


Fig. 5 : The four stress states determined by computing tensors from striated faults observed in cores of the EPSI borehole (lower Schmidt projection).

Diagram	A	B	C	D
Stress stage	N-S Compr.	E-W Extens.	NE-SW Compr.	NW-SE Compr.
Number of faults	40	40	22	17
$\sigma_1$ (dip dir. - dip)	19 - 3	26 - 84	254 - 3	301 - 22
$\sigma_2$ (dip dir. - dip)	128 - 82	186 - 6	348 - 53	65 - 54
$\sigma_3$ (dip dir. - dip)	289 - 8	276 - 2	162 - 36	199 - 27
$\Phi$	0.491	0.42	0.38	0.20
Mean angle	24	19	20	19
Mean RUP	72%	40%	73%	63%
Angle distribution				
RUP distribution				

E	Remaining faults	21 faults = 15%
---	------------------	-----------------

Tab. 2 : Parameters of stress computation.

A, B, C, D, E : diagrams corresponding to the stress state and remaining faults shown in fig. 5.

$\sigma_1$ : trend and plunge of maximum principal stress axis;  $\sigma_2$ : trend and plunge of intermediate principal stress axis;  $\sigma_3$ : trend and plunge of minimum principal stress axis (compressive stress is positive).  $\Phi$ : ratio of principal stress differences  $\Phi = (\sigma_2 - \sigma_3)/(\sigma_1 - \sigma_3)$ . Angle: average angle between actual striae and computed shear, used as quality estimator of the inversion method for computing the stress tensor (ranging from 0° to 90° as misfit increases). RUP: ratio defined by Angelier (1990) as an additional quality estimator (in %, ranging from 0 to 200% as misfit increases).

- NE-SW compression (Fig. 5-C), deduced from 22 strike slip faults. Note that dextral faults strike approximately N-S, whereas sinistral ones strike E-W. The  $\sigma_2$  and  $\sigma_3$  have significant plunges, while the  $\sigma_1$  axis is horizontal. Oblique slips are frequently observed on normal faults, and most fault and slip orientations do not fit the requirements for conjugate sets. This confirms that many of these faults were in fact inherited from older fracture surfaces.

- NW-SE compression (Fig. 5-D), deduced from 17 strike slip faults. Note that sinistral faults strike N-S, whereas dextral ones strike E-W. The plunges of stress axes are similar to those of the regime previously discussed, but the trends are quite different.

The fault surfaces visible in the cores are necessarily much smaller than those usually observed in outcrop (the core diameter being either 96 mm or 56 mm). Despite this small size, some faults showed two contrasting sets of



striations indicating successive slips in different directions. Such chronological data remained scarce, so that the chronology of faulting events could not be accurately established. Villemin (1986), in a regional study of the Rhingraben region, suggests the following chronology of events for the Cenozoic paleostress evolution: (1) N-S compression, (2) E-W extension, (3) NE-SW compression and (4) NW-SE compression. If we assume that the same events are observed in the granite basement of Soultz, the order adopted in the above presentation (Fig. 5) reflects the chronological order of events (Dezayes *et al.*, 1993).

## 2-2 Analysis of fractures without striae

The distribution of all fractures with depth displays four sections zones with high fracture densities (Fig. 6).

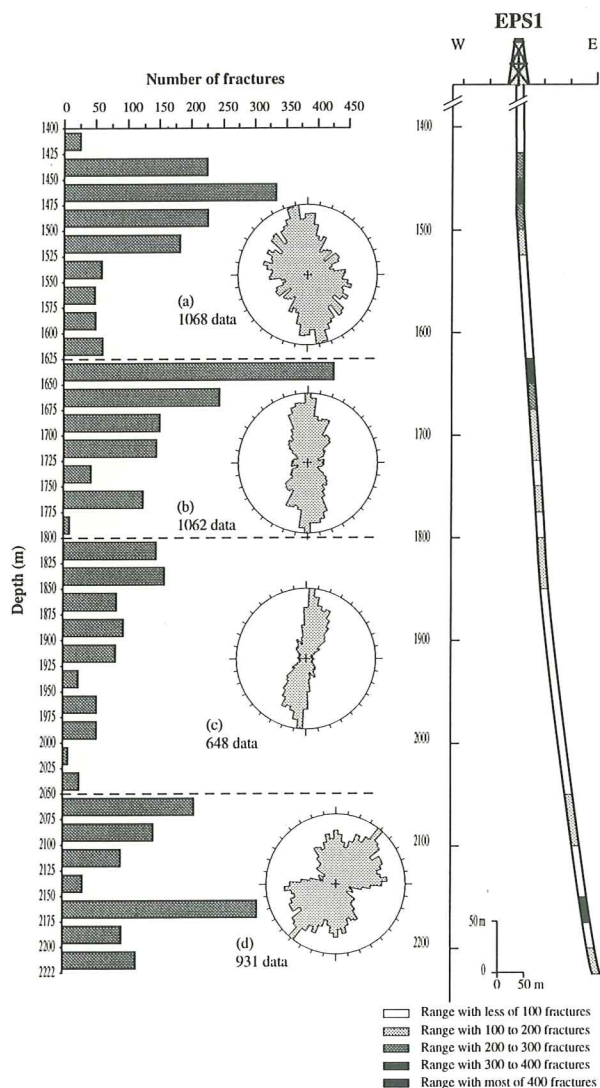


Fig. 6 : Number of natural and induced fractures by range of 25 m depth with the rose diagram corresponding to four sections of the EPS1 borehole. From top to bottom respectively 1400-1600 m, 1600-1800 m, 1800-2050 m, 2050-2200 m (rose diameter proportional to the maximum frequency, angle interval of 5°).

The rose diagrams for these zones show that the mean strike rotates clockwise as depth increases, the average strike changing from N170°E - N180°E in the upper zone (Fig. 6-a), to N220°E near the bottom of the well (Fig. 6-d).

Both natural and induced fractures have been recognized in the cores (§ 1-1-1). Each fracture type shows two sets (Fig. 7). Whereas the natural fracture sets are symmetrical (Fig. 7-A), the induced fracture sets are not (Fig. 7-B). The dip directions of both fracture types grouped into the 4 depth classes have been analysed (Fig. 8). For the natural fractures, the angle between the orientations of the two sets decreases as the depth increases from 1400 to 2050 m (Fig. 8-1N, 2N and 3N). Below this depth, only the W-dipping set is present (Fig. 8-4N). The density of induced fractures, which is rather small at the top of the granite (Fig. 8-1I), increases with depth to 2050 m (Fig.

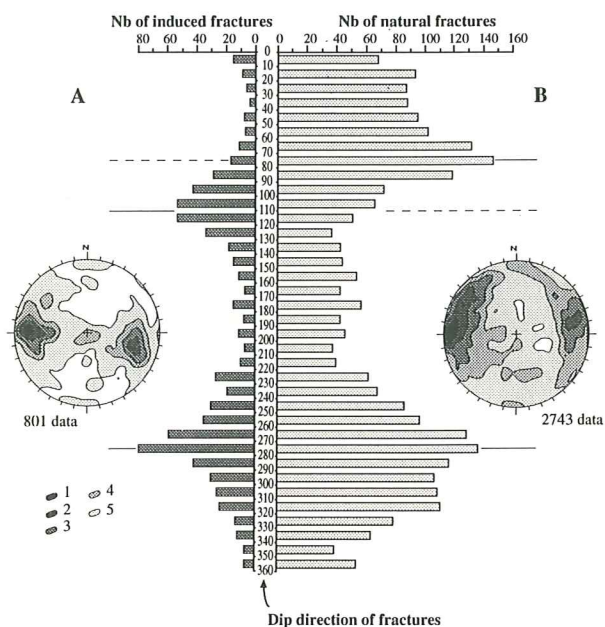


Fig. 7 : Histogram of number of fractures vs dip directions of induced (A) and natural (B) fractures observed in cores of the EPS1 borehole, with corresponding contoured density diagrams (lower Schmidt projection); 1, 2, 3, 4, 5: 90%, 70%, 50%, 30%, 10% of the maximum frequency respectively.

8-2I and 3I) and then decreases at large depths (Fig. 8-4I). The angular difference between the dip directions of both sets is practically constant with depth, but a rotation of the average dip direction from N90°E-N260°E (Fig. 8-2I), through N100°E-N270°E (Fig. 8-3I) to N140°E-N310°E (Fig. 8-4I) is observed. This rotation may correspond to a local variation of the recent stress orientation with depth.

## 2-3 Analysis of fractures observed on borehole imagery

Considering the shape of fractures identified from borehole images, as well as their organization in terms of strikes and dips and the comparison with the cores, allows to a certain extent distinction between natural fractures (due to

regional tectonic events) and induced fractures (due to drilling). In the Soultz boreholes, from this analysis, most open fractures (type 1) and closed ones (type 2) are of tectonic origin. In contrast, the other fracture types, half-fractures (type 3), "en échelon" fractures (type 4) and vertical long fractures (type 5), are probably induced (these five types having been defined earlier).

observed in this well affect the sedimentary cover and are not numerous (45 fractures; Tab. 3), the comparison with the other data is not considered significant.

For the EPS1 borehole, the mean strike of natural fractures (N30°E-50°E; Tab. 3) deduced from images is similar to that deduced from core analysis, but dispersion is much greater in the cores than from image analysis.

Type of fractures		EPS1 (1845-1960 m.) (n=246)	GPK1 (1645-1745 m.) (n=308)	P4550 (1260-1295 m.) (n=45)
Natural fractures	Total number	n = 14	n = 48	n = 14
	Strike of types 1	N 30°E-50°E	N 20°E	N 170°E
	Strike of types 2		N 80°E	.
Induced fractures	Total number	n = 232	n = 260	n = 31
	Strike of types 3	N 40°E	N 50°E-80°E	N 160°E
	Strike of types 4	N 150°E	N 60°E-80°E	N 70°E-90°E
	Strike of types 5	N 120°E	N 130°E-150°E	
All the data	Total number	n = 246	n = 308	n = 45
	Mean strike	N 30°E and N 150°E	N 70°E	N 170°E

Table 3 : Dominant strikes of fractures visible on BHTV images (n: number of fractures).

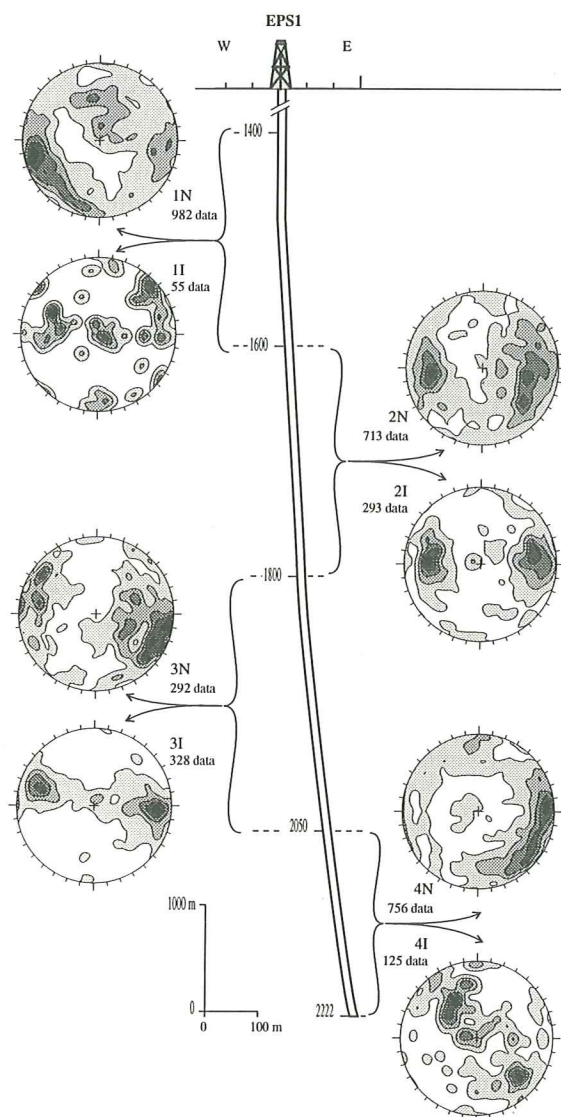


Fig. 8 : Contoured diagrams (lower Schmidt projection) of natural and induced fractures observed in four depth sections of the EPS1 borehole (legend as in fig. 7).

1N, natural fractures from 1400 to 1600 m depth; 1I, induced fractures from 1400 to 1600 m depth; 2N, natural fractures from 1600 to 1800 m depth; 2I, induced fractures from 1600 to 1800 m depth; 3N, natural fractures from 1800 to 2050 m depth; 3I, induced fractures from 1800 to 2050 m depth; 4N, natural fractures from 2050 to 2200 m depth; 4I, induced fractures from 2050 to 2200 m depth.

There is close agreement between fracture orientations recognized in the granite granite of both the EPS1 and GPK1 boreholes (Tab. 3). Note that in the P4550 well, the orientations differ: however, because the fractures

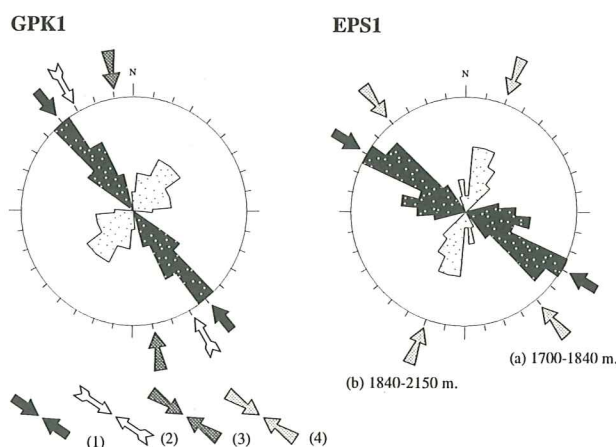


Fig. 9 : Circular rose histograms of azimuths of vertical traces on BHTV images for the GPK1 (A) and EPS1 (B) boreholes and most probable orientation of corresponding  $\sigma_{Hmax}$ . Data collected from the segment of GPK1 located between 1645 and 1747 m (17 measurements) and the segment of EPS1 located between 1845 and 1960 m (20 measurements).

(1),  $\sigma_{Hmax}$  deduced from the highest frequency of vertical fractures BHTV images; (2), Present-day horizontal maximal stress ( $\sigma_H$ ) from in-situ measurements, GPK1 borehole (from Rummel and Baumgartner, 1991); (3),  $\sigma_{Hmax}$  deduced from the highest frequency of vertical fractures on BHTV images in the GPK1 borehole (from Tenzer et al., 1991); (4),  $\sigma_{Hmax}$  deduced from the highest frequency of vertical fractures on BHTV images, EPS1 borehole (from Tenzer et al., 1992).



This analysis of fracture orientation from images has been carried out in part of the boreholes only. A complete description has been carried out by Tenzer *et al.* (1991) for GPK1 and Tenzer *et al.* (1992) for EPS1. The principal directions of the natural discontinuities and the vertical fractures of GPK1 are striking N150°E-170°E and N160°E-180°E respectively (Fig. 9-A). In EPS1, the dominant strike for the natural discontinuities is N30°E and while the vertical fractures trend N140°E-160°E from 1700 to 1840 m and N20°E-30°E from 1860 to 2150 m (fig. 9-B).

### 3- Data interpretation and conclusions

The different methods used in this work allowed interpretation of fracture and fault systems in terms of stresses acting in the granite from the HDR drillsite at Soultz. Such an approach, essentially based on core analysis, results in a better understanding of the tectonic history than a simple geometrical description. The relation between the natural and induced fractures needs more detailed investigation.

#### 3-1 Paleostresses and present-day stress

Summarizing the results previously discussed, our analysis of the striated faults observed in the cores lead to identify the following succession of stress states (Fig. 5) :

- (1) N20°E compression, with  $\sigma_2$  nearly vertical;
- (2) N100°E extension, with  $\sigma_1$  nearly vertical;
- (3) N80°E compression, with  $\sigma_2$  steeply plunging;
- (4) N120°E compression, with  $\sigma_2$  steeply plunging.

The N120°E compression may correspond to the recent and present-day stress (Villemin, 1986). The orientation of the maximum horizontal principal stress axis,  $\sigma_{H \max}$ , suggested by induced fractures in the EPS1 borehole (Fig. 9-B) differs by an amount of 20° from the regional present-day stress deduced from microtectonic studies (Villemin, 1986). This variation seems to be due to a local deviation of the regional stress field.

In the borehole imagery, different types of fractures were identified and grouped into sets defined on a geometrical basis. The long fractures (type 5) are interpreted as hydraulic fractures induced during drilling and directly related to the orientation of the present-day maximum horizontal principal stress (Tenzer *et al.*, 1991). In this case, the maximum horizontal principal stress axis in the GPK1 borehole is N140°E-160°E, in the depth range of 1645 to 1745 m (Fig. 9-A), whereas in the EPS1 borehole it is N120°E, in the depth range of 1845 to 1960 m (Fig. 9-B). These results suggest that significant stress perturbations may occur depending on the fault block structure, resulting in variations in the trend of the maximum horizontal stress as large as 20-40°.

#### 3-2 Tectonic evolution of fracture systems

Two methods have been used in order to characterize fractures: a direct method based on observation of fractures in the cores, and an indirect method based on observations of borehole images. The use of both methods permits us to have an overall view of the fracture system.

The analysis of cores enables two types of fractures to be distinguished: natural fractures and fractures induced by the drilling. For instance, the analysis of the dip direction of induced fractures shows a change in dominant trends with depth at 2000 m, which is not the case for the natural fractures (Fig. 8-I). This rotation could be interpreted as a perturbation of stresses with depth, probably due to the vicinity of a main fault. This fault could be the discontinuity zone observed at about 2200 m in EPS1. However no significant seismic activity is observed on this fault.

In the core of the totality of granite (between 1400 and 2220 m), a total of 4100 fractures have been observed, whereas less than 500 fractures appear on the borehole images (Tenzer *et al.*, 1992) on the same range. This difference results from a too small electrical or sonic contrast on the intersection between fault and core. This contrast remains too small in most cases, to be detected by the logging imagery tools whereas they are clearly identifiable in cores.

#### 3-3 Natural and induced fractures

The comparison between natural and induced fractures in terms of contoured orientation diagrams (Fig. 8) shows different orientations of the main sets. In several cases (especially in the Fig. 8-1 and 8-2), the main orientations of induced fractures take place, in the stereoplot, where there are few many natural fractures. The fractures induced by the drilling can be distinguished from the oldest ones. However, only part of the inherited fractures, on which  $\sigma_n$  is at maximum, can be re-opened under the present state of stress, during drilling. Such fractures may have a more variety of orientations than if they are purely neoformed. We disregard this third category of fractures, because they could not be distinguished when the cores have been observed.

The distribution of natural fractures systems suggests in most cases the existence of conjugate sets (Anderson, 1951), implying that many fractures were shear surfaces. However, most of the conjugate systems do not correspond to clearly defined paleostresses; in particular, these inferred paleostresses were not revealed by stress tensor computations based on striated fault data. We infer that such conjugate systems (and the related paleostresses) were in fact older than the fault patterns discussed in an earlier section. In other words, numerous fault slip (as shown in Fig. 5) result of reactivation on earlier fracture systems, the original slickenside lineations being scarce or erased.

*Acknowledgements.* This research was carried out under the auspices of the European Hot Dry Rock Project funded by Commission of the European Communities (DG XII). Geological investigations were supported in part by the BRGM and in part by the Agence de

l'Environnement et de la Maîtrise de l'Energie (ADEME). The authors thank Henry Charlesworth (University of Alberta) for helpful comments.

## References

- Anderson E M (1951) The dynamics of faulting. Oliver & Boyd ed., Edimbourg.
- Angelier J (1979) Néotectonique de l'arc égéen. Thèse d'état de l'Université Paris VI, Soc. Géol. Nord, 3.
- Angelier J (1990) Inversion of field data in fault tectonics to obtain the regional stress-III. A new rapid direct inversion method by analytical means. *Geophys. J. Int.* 103: 363-376.
- Angelier J (1991) Inversion directe et recherche 4-D : comparaison physique et mathématique de deux modes de détermination des tenseurs des paléocontraintes en tectonique de failles. *C. R. Acad. Sci. Paris* 312 II: 1213-1218.
- Dezayes C (1992) Etude de la fracturation dans les forages géothermiques de Soultz-sous-Forêts (Alsace, France). Unpublished memoir, Université de Savoie.
- Dezayes C, Villemain T, Genter A, Traineau H & Angelier J (1993) Paleostress analysis from fault and fracture geometry in the Hot Dry Rock boreholes at Soultz-sous-Forêts (Rhine graben). European Union of Geosciences EUG VII 4-8 April 1993, Terra Nova 5: 217.
- Genter A & Traineau H (1991) Geological survey of the HDR borehole EPS1, Soultz-sous-Forêts, Alsace, France. Open File Report, BRGM-IMRG R32433.
- Genter A & Traineau H (1992) Borehole EPS1, Alsace, France : preliminary geological results from granite core analyses for Hot Dry Rock research. *Scientific Drilling* 3: 205-214.
- Genter A, Traineau H, Dezayes C, Elsass P, Ledesert B, Meunier A & Villemain T (1994) Fracture analysis and reservoir characterization of the granitic basement in the HDR Soultz project (France). *Geotherm. Sci. & Tech.* in press.
- Kappelmeyer O, Gerard A, Schloemer W, Ferrandes R, Rummel F & Benderitter Y (1991) European HDR Project at Soultz-sous-Forêts, general presentation. *Geotherm. Sci. & Tech.* 2(4): 263-289.
- Rummel F & Baumgartner J (1991) Hydraulic fracturation measurements in the GPK1 borehole, Soultz-sous-Forêts. *Geotherm. Sci. & Tech.* 3(1-4): 119-148.
- Schnaebelé R (1948) Monographie géologique du champ pétrolifère de Pechelbronn. Mémoire du service de la carte géologique d'Alsace et de Lorraine 7.
- Shellschmidt R & Schulz R (1991) Hydrothermic studies in the Hot Dry Rock project at Soultz-sous-Forêts. *Geotherm. Sci. & Tech.* 3: 217-238.
- Tenzer H, Budeus P & Shellschmidt R (1992) Fracture analyses in Hot Dry Rock drillholes at Soultz and Urach by borehole televiwer measurements. *Geothermal Resources Council Transactions* 19: 317-321.
- Tenzer H, Mastin L & Heinemann B (1991) Determination of planar discontinuities and borehole geometry in the crystalline rock of borehole GPK1 at Soultz-sous-Forêts. *Geotherm. Sci. & Tech.* 3(1-4) : 31-67.
- Traineau H, Budeus P, Genter A & Tenzer H (1992) Core data and well-logging responses in a deep granite body destined for HDR experiments (Soultz, France). Document du BRGM 213: 243.
- Villemain T (1986) La chronologie des événements tectoniques dans le Nord-Ouest de la France et le Sud-Est de l'Allemagne du Permien à l'actuel. *C. R. Acad. Sci. Paris* 303 II 18: 1685-1690.



